J. Fluid Mech. (2014), *vol.* 756, *pp.* 354–383. © Cambridge University Press 2014
doi:10.1017/jfm.2014.458

Flow structure on a simultaneously pitching and rotating wing

M. Bross[1] **and D. Rockwell**[1,†]

[1]Department of Mechanical Engineering and Mechanics, Lehigh University, Bethlehem, PA 18015, USA

(Received 21 January 2014; revised 23 July 2014; accepted 4 August 2014;
first published online 2 September 2014)

A technique of particle image velocimetry is employed to characterize the three-dimensional flow structure on a wing subjected to simultaneous pitch-up and rotational motions. Distinctive vortical structures arise, relative to the well-known patterns on a wing undergoing either pure pitch-up or pure rotation. The features associated with these simultaneous motions include: stabilization of the large-scale vortex generated at the leading edge, which, for pure pitch-up motion, rapidly departs from the leading-edge region; preservation of the coherent vortex system involving both the tip vortex and the leading-edge vortex (LEV), which is severely degraded for pure rotational motion; and rapid relaxation of the flow structure upon termination of the pitch-up component, whereby the relaxed flow converges to a similar state irrespective of the pitch rate. Three-dimensional surfaces of iso-Q and helicity are employed in conjunction with sectional representations of spanwise vorticity, velocity and vorticity flux to interpret the flow physics.

Key words: aerodynamics, biological fluid dynamics, swimming/flying

1. Introduction

The flow structure and loading on wings undergoing unsteady manoeuvres has been of major interest in recent years. Research in the area of low-Reynolds-number, unsteady flight is directly relevant to the design of small unmanned air vehicles. A central concept involves flapping wings, which are characterized by large-amplitude rotation, pitching, and/or plunging. Several reviews of flapping wings are provided by Sane (2003), Lehmann & Dickinson (1998), and Shyy *et al.* (2010). Of specific interest herein are investigations related to the flow structure and loading due to pure pitch-up, combined pitch-up–rotation and pure rotation of a wing, with emphasis on finite-span wings having low aspect ratio.

1.1. *Flow structure due to pitch-up motion*

The unsteady flow separation on an aerofoil or other lifting surface executing time-dependent motion, such as large-amplitude pitching motion, induces a large-scale vortical structure associated with dynamic stall (McCroskey 1982). The overviews of McCroskey (1982) and Ekaterinaris & Platzer (1998) indicate that dynamic stall

---

[†] Email address for correspondence: dor0@lehigh.edu

was initially identified in helicopter and turbomachinery applications. Little is known, however, of the flow structure arising from large-amplitude, non-periodic pitch-up motion of a wing with finite aspect ratio.

The seminal computational study of Visbal & Shang (1989) examined an aerofoil undergoing large-amplitude pitch-up motion. They investigated the two-dimensional, low-Reynolds-number ($Re = 104$) flow past an NACA 0015 aerofoil pitched at constant rate to a 60° angle of attack. A parametric study revealed the effects of pitch rate and location of the pivot axis on the flow structure and aerodynamic loading on a rapidly pitching aerofoil. Visbal & Shang (1989) identified the formation and development of the dynamic-stall vortex and established a strong connection between the maximum lift created by the aerofoil and the pitch rate and pitch axis location.

Shih *et al.* (1992) experimentally characterized the flow past a two-dimensional pitching NACA 0012 aerofoil to a maximum angle of attack of $\alpha = 30^\circ$ at a low Reynolds number, $Re = 5000$. They employed particle image velocimetry to visualize the formation and growth of leading- and trailing-edge vortex structures during the pitch-up manoeuvre. Shih *et al.* (1992) concluded that leading-edge flow separation occurs when $\alpha > 20^\circ$, resulting in a local accumulation of vorticity, which develops into a leading-edge vortex (LEV) having a scale of one-half the wing chord. Using a vortex point identification technique, they showed that this large-scale vortex structure originates completely from the leading edge during the early part of the pitch-up manoeuvre.

Eldredge & Wang (2010) investigated computationally the effects of reduced pitch rate ($K = \dot{\alpha}_0 C/(2U_\infty) = 0.05$ and 0.1) and pitch axis location ($x_p/C = 0$, 0.25, and 0.5) on the flow structure and loading of a two-dimensional flat plate undergoing a linear pitch-up manoeuvre. The flat plate pitched to a maximum angle of attack of $\alpha = 45^\circ$ in a uniform flow; the Reynolds number based on the plate chord was $Re = 1000$. Their results suggest a dependence of the maximum lift and drag coefficients on the values of K and x_p/C. They also noted that, for a given value of x_p/C, and for increasing K, there appeared an additional delay in the development of the LEV and an increase in its overall scale.

Garmann & Visbal (2011) performed a three-dimensional simulation of the flow structure along a rapidly pitching plate. They studied the effect of Reynolds number ($Re = 5000$–$40\,000$), spanwise extent (span/chord $= b/C = 0.1$, 0.2, 0.4, and 0.8), and initial acceleration on the flow structure and aerodynamic loading on the plate during the pitch-up manoeuvre. While varying the spanwise extent, they observed that force magnitudes and contour patterns of constant spanwise vorticity appeared to be insensitive to this change. The development of the dynamic-stall vortex also appeared to be insensitive to a change in initial acceleration. Moreover, Garmann & Visbal (2011) showed, via volume representations of iso-Q surfaces, that the aerodynamic loading and flow structure exhibited relative insensitivity to changes of the Reynolds number. The only distinction was a loss in coherence of the flow structure with increasing Reynolds number.

Granlund, Ol & Bernal (2011) performed an experimental investigation involving pitching low-aspect-ratio ($AR = 2$) rectangular and elliptical flat plates at a low Reynolds number (10 000). The aerodynamic loading for both planforms was measured as each plate pitched from 0 to 90° at reduced pitch rates of $K = 0.03$ and 0.2. Also Granlund *et al.* (2011) used dye visualization to characterize the flow structure for each planform at $K = 0.2$, while varying the pivot points, $x/C = 0$, 0.5, and 1. Their results showed that there were relativity minor differences in the flow structure and loading between the planforms. They also showed that the non-circulatory forces associated with increases in magnitude of the lift coefficients can be attributed to an increase in pitch rate. Moreover, the growth and subsequent shedding of the LEV appeared to correlate with peaks of the lift coefficients.

Yilmaz, Ol & Rockwell (2010) also addressed three-dimensional effects via flow visualization (dye injection). They explored the flow patterns due to unsteady motion of a rapidly pitching or plunging low-aspect-ratio ($AR = 2$) flat plate. Focusing on the pitch-up and return motion, Yilmaz *et al.* (2010) explored alterations of the flow structure due to variations of the reduced pitch rate ($K = 0.1$, 0.2, 0.35) and the pitch pivot axis ($x/C = 0$, 0.25, 0.5, 0.75, and 1); in all cases, the Reynolds number was $Re = 10\,000$. One of results of the flow visualization was a delay in formation of the LEV due to a change in pitch rate for a fixed location of the pitch axis. Yilmaz *et al.* (2010) also qualitatively identified the highly three-dimensional nature of the flow structure on finite wings undergoing pitch-up manoeuvres.

Yilmaz & Rockwell (2012) employed quantitative flow visualization in the form of stereo particle image velocimetry (SPIV) to construct the three-dimensional flow patterns on a finite-span wing due to pure pitch-up motion. Their investigation addressed the flow structure along low-aspect-ratio rectangular and elliptical wings ($AR = 2$) undergoing pitch-up motion to high angle of attack ($\alpha = 45^\circ$); the value of Reynolds number was $Re = 10\,000$ based on wing chord. For a fixed reduced pitch rate ($K = 0.098$) and pitch axis location ($x/C = 0.25$), the goal was to characterize the vortex structure via volume-based representations, so that the time evolution of the flow structure could be defined during the pitching manoeuvre. The high-resolution volume representations given by Yilmaz & Rockwell (2012) indicated that evolution of the flow structure was distinctly different for the elliptical and rectangular plates, but after sufficient relaxation time, comparable three-dimensional structures existed.

More recently, Hartloper, Kinzel & Rival (2013) used a three-dimensional particle tracking velocimety (3D-PTV) visualization technique as well as force measurements to characterize the flow structure and loading along a nominally two-dimensional (infinite-aspect-ratio) plate and a low-aspect-ratio ($AR = 4$) rectangular plate. The plates were subjected to pitching motion, in the form of a half-cosine velocity profile, to a maximum angle of attack of 45°. The reduced pitch rates were $K = 0.26$ and 1.57. Hartloper *et al.* (2013) reached several conclusions about the growth of the leading-edge and tip vortices. Namely, the growth of the LEV for the infinite plate was independent of pitch angle α, whereas for the low-aspect-ratio plate, the growth of the LEV was more correlated with the convective time scale, $t^* = tU_\infty/C$. They also concluded that the leading-edge and tip vortices grow independently of each other. However, the tip vortex influences the dynamics of the LEV, resulting in an arch-shaped vortex structure near the midplane of the wing, as first computed by Visbal (2011) and experimentally examined by Yilmaz & Rockwell (2012).

The influence of the LEV on the lift generated by a rapidly pitching wing was also examined by Zhang & Schluter (2012). Using numerical methods, they investigated the lift generated by a rapidly pitching $AR = 2$ flat plate at chord-based Reynolds numbers from $Re = 440$ to $21\,000$. They showed that, for $Re < 2000$, viscous effects result in a decrease of aerodynamic efficiency. However, for higher Reynolds number ($Re > 2000$), the lift-to-drag ratio based on the maximum instantaneous values during generation of the LEV appears to be insensitive to Reynolds number. This observation may explain why a vast range of biological flyers employ an LEV for lift generation.

1.2. *Flow structure due to rotation*

In the presence of wing rotation, angular, centripetal and Coriolis accelerations influence the spanwise flow and vortex structure on a flapping wing. Lentink &

Dickinson (2009*a*) provide a conceptual framework for the influence of an LEV on aerodynamic performance of flapping wings, as well as related scaling phenomena. Of specific interest herein are investigations related to pure rotation at fixed angle of attack.

Investigating biological planforms, Lentink & Dickinson (2009*b*), Dickson & Dickinson (2004) and Poelma, Dickson & Dickinson (2006) examined models of dynamically scaled *Drosophila melanogaster* wings while accounting for Reynolds number effects, aerodynamic loading, and wing kinematics. Lentink & Dickinson (2009*b*) considered a rotating wing representation of *D. melanogaster* with fixed angles of attack $\alpha = 36^\circ$ and 45° for $Re = 110$ and 1400. Using bubble visualization, they demonstrated the existence of a stable LEV, and attributed the vortex stability to Coriolis and centripetal fluid accelerations. Dickson & Dickinson (2004) classified the effect of flight parameters on the loading of a dynamically scaled *D. melanogaster* wing with AR = span/(mean chord) ≈ 4 rotating at constant angle of attack at $Re = 140$; the flow structure was not addressed. The Dickson & Dickinson (2004) results showed that the amplitude of the lift and drag coefficients was not only dependent on the angle of attack but also on the tip velocity ratio, which is the ratio of the chordwise components of flow velocity at the wing tip due to translation and revolution (i.e. infinite tip velocity ratio represents a translating wing). Moreover, Poelma *et al.* (2006) characterized the three-dimensional structure on the model *D. melanogaster* wing, and created volume representations of vorticity. They observed that, after the initial stage of rotation, strong spanwise flow exists and is key to the stability of the flow field around the wing.

The extensive work on rotating wings also includes investigations involving simple geometric planforms. These investigations mainly involve variations of aspect ratio and Reynolds number at a fixed angle of attack. Ansari *et al.* (2009) demonstrated the effect of Reynolds number on the structure of the LEV on a low-aspect-ratio ($AR = 2.5$) rectangular wing undergoing rotation at a fixed angle of attack $\alpha = 45^\circ$ in quiescent flow. Flow visualization at different sectional cuts along the wing revealed how different Reynolds numbers ($Re = 500$ and 15 000) create a similar structure of the LEV during the start-up of wing rotation. They observed, however, a slight loss of coherence of the vortex structure and onset of more pronounced Helmholtz instabilities at the larger Reynolds number.

Kim & Gharib (2010) examined the three-dimensional flow structure and loading on a rotating flat plate for Reynolds numbers between 60 and 8800. They demonstrated a conical and stable structure of the LEV along with an established spanwise flow along a plate of aspect ratio $AR = 2$. Moreover, they observed a decrease in the impulse and lift forces acting on the wing with a decrease in Reynolds number.

Ozen & Rockwell (2011) used quantitative imaging to determine the structure and retention of the LEV on an aspect ratio $AR = 1$ rectangular wing rotating at fixed angle of attack. Their experiments led to the observation that for a given angle of attack, the scale and form of the vortex was relatively insensitive to Reynolds number in the range $Re = 5400$–21 600. In addition, they described the presence of strong spanwise (axial) flow and downwash corresponding to the stable LEV on the leeward side of the wing.

Investigating the effects of aspect ratio, Carr, Chen & Ringuette (2013) highlighted the differences in the tip-vortex behaviour for rotating rectangular plates at a fixed angle of attack. At $Re = 5000$, Carr *et al.* (2013) demonstrated, through quantitative flow visualization, that the LEV is less coherent near the tip of a wing having an aspect ratio $AR = 4$, compared to $AR = 2$. The tip vortex enhanced the coherence of the

LEV in this region on the $AR=2$ wing, relative to the $AR=4$ wing. Also investigating $AR=2$ and 4 plates, Wojcik & Buchholz (2014) compared sectional cuts of the flow structure along the span of a rotating rectangular plate at various Reynolds numbers, angles of attack and phases of rotation. They observed an increase in the strength of the LEV as the Reynolds number changed from $Re=4000$ to 16 000. However, similar trends in vortex development were observed for both aspect ratios over the range of Reynolds number.

Garmann, Visbal & Orkwis (2013) computed the vortex structure and aerodynamic loading on a rotating rectangular flat plate of aspect ratio $AR=1$ for a range of Reynolds numbers between 200 and 60 000. These numerical simulations were shown to be in good agreement with the experimental results of Ozen & Rockwell (2011) for cases where values of parameters were matched. Namely, an attached LEV persisted to large angle of rotation.

More recently Garmann & Visbal (2014) computed the flow structure and aerodynamic performance of revolving wings of aspect ratio 1, 2, 3 and 4. Maintaining a Reynolds number at the root of 1000 for each aspect ratio, the three-dimensional flow structure was visualized with isosurfaces of total pressure and Q-criterion. These visualizations show the presence of a stable coherent vortex structure shortly after the onset of motion for all aspect ratios. The scale and eventual breakdown of the LEV was sensitive to distance from the axis of rotation, i.e. aspect ratio. Garmann & Visbal (2014) also computed coefficients of lift and drag throughout the motion. For $AR=2$ and 4, C_D and C_L initially increase, eventually plateauing at larger rotation angles. The $AR=1$ wing exhibits the same trend in performance but does not quite reach the higher plateau peak that C_D and C_L attained for larger-aspect-ratio wings. In addition, analysis of the centrifugal, Coriolis, and pressure gradient forces for all aspect ratios at 25 % span showed that pressure gradient and centrifugal terms were mainly responsible for the large regions of outboard flow on the suction side of the wing. They also noted that the normal (with respect to wing surface) component of the Coriolis force shows a moderate contribution in the core and at the base of the LEV, suggesting that the Coriolis force hinders attachment of the LEV.

Ozen & Rockwell (2012) addressed the three-dimensional flow structure on a wing of aspect ratio $AR=2$ during the early and late stages of rotation. They employed SPIV to characterize the relationship between volumetric representations of the structure of the LEV and sectional concentrations of both chordwise and spanwise oriented vorticity, as well as spanwise flow. In turn, these features were related to the coherence of the tip and root vortices.

Bross, Ozen & Rockwell (2013) examined the three-dimensional flow structure on a rotating rectangular wing having an aspect ratio $AR=2$ in the presence of incident free stream. This investigation employed quantitative imaging (SPIV) to characterize the effect of advance ratio J (ratio of tip to free-stream velocity) on the development of the flow structure along, and in the wake of, a rotating wing maintained at a constant value of effective angle of attack. The results indicate that similar structures such as leading, tip, and root vortices exist at the smallest and largest values of J. At higher values of J, however, the Kelvin–Helmholtz instability in the wake region downstream of the trailing edge became prevalent.

Cheng *et al.* (2013) quantified the flow patterns along wings revolving at high angle of attack in quiescent fluid using a volume PIV approach. From flow field data on an $AR=7$ (two times the wing span/mean chord length) wing at a 45° angle attack, rotating at $Re=220$, they calculated terms in the vorticity transport equation in order to identify the underlying vortex dynamics associated with a stable LEV.

Their findings suggest that, at this very low Reynolds number, convection in the radial and vertical directions is of importance, relative to convection in the spanwise direction, in determining the stability of the leading edge.

Biological flyers that inspire the design of micro air vehicles typically employ a combination of pitching, plunging, and rotational motions in order to optimize the aerodynamic performance. The present investigation focuses on the detailed flow structure along a low-aspect-ratio wing undergoing a prevalent combination of motions, i.e. combined pitch-up and rotation, in comparison with simple pitch-up and pure rotation. These manoeuvres were chosen to represent generic unsteady motions, and are broadly applicable to a range of applications including a rotating helicopter blade or propeller. Within the category of bio-inspired phenomena, the combination of pitch-up and rotation is most akin to a perching-type manoeuvre of a biological flyer. Of particular interest is the effect of rotation on the evolution of the flow structure induced by pitch-up motion. Quantitative imaging is employed to characterize the detailed three-dimensional flow structure.

2. Experimental systems and techniques

Experiments for combined pitch-up–rotation and pure rotation were performed in a free-surface water channel with an overall test section length of 4877 mm, a width of 927 mm, and a depth of 610 mm. Figure 1 shows isometric and side views of the rotating and pitching wing system. A flat plate with sharp (rectangular) edges was used as the wing model. The transparent wing has an aspect ratio $AR = b/C = 2$, a chord $C = 38.1$ mm, a span $b = 78.1$ mm and a thickness $t = 2.8$ mm. The root of the wing is connected to a rotating centrebody of diameter 31.75 mm with a rod, which had a diameter of 3.17 mm at the wing root. The distance between the surface of the rotating body and the root of the wing was maintained at 19.05 mm while the distance from the centre of rotation to the root of the wing was $r_0 = 34.93$ mm. The plane representing the laser sheet intersects the wing in the chordwise direction. The angle of rotation and the pitch angle of the wing are defined respectively as ϕ and α.

These experiments were performed in quiescent fluid. An original rotating and pitching apparatus was designed and constructed for these experiments as shown in figure 2. One stepper motor drove a rotation stage while another stepper motor drove a system of belts and chain linkage, which were located inside the rotating shaft, controlling the pitching motion. The stepper motors were driven by micro stepper drivers controlled through LabView software. Encoders attached to the stepper motors were set to indicate the error of ±2 steps. Additionally the mechanical lag in the components was estimated to be 1° and 2° respectively for the pitching and rotation motions.

The wing was rotated about the y-axis at an angular velocity $\dot{\phi} = 2.79\ \mathrm{rad\ s^{-1}}$, corresponding to values of tip velocity $V_{tip} = 310\ \mathrm{mm\ s^{-1}}$ and velocity at the radius of gyration $V_{rg} = 204\ \mathrm{mm\ s^{-1}}$. The Reynolds number based on the tip velocity was $Re = 11\,776$. The reduced pitch rate had values of $K = \dot{\alpha}C/(2V_{rg}) = 0.393$, 0.262, and 0.098. Correspondingly, the reduced rotation rate had a value of $\varOmega = \dot{\phi}C/(2V_{rg}) = 0.261$. For the experiments involving rotation, the wing reached a constant angular (rotation) velocity $\dot{\phi}$ at $\phi = 25.6°$ corresponding to $\tau = 0.86$, where τ is the convective time scale $\tau = tV_{rg}/C$. Similarly, for experiments involving pitch-up motion, the wing reached constant angular (pitching) velocity $\dot{\alpha}$ at $\alpha = 9.7°$, 14.5°, 19.3°, i.e. $\tau = 0.83$, 0.48 and 0.43, for $K = 0.098$, 0.262, and 0.393 respectively. Slight smoothing, corresponding to a value of the parameter $a = 700$ of Eldredge &

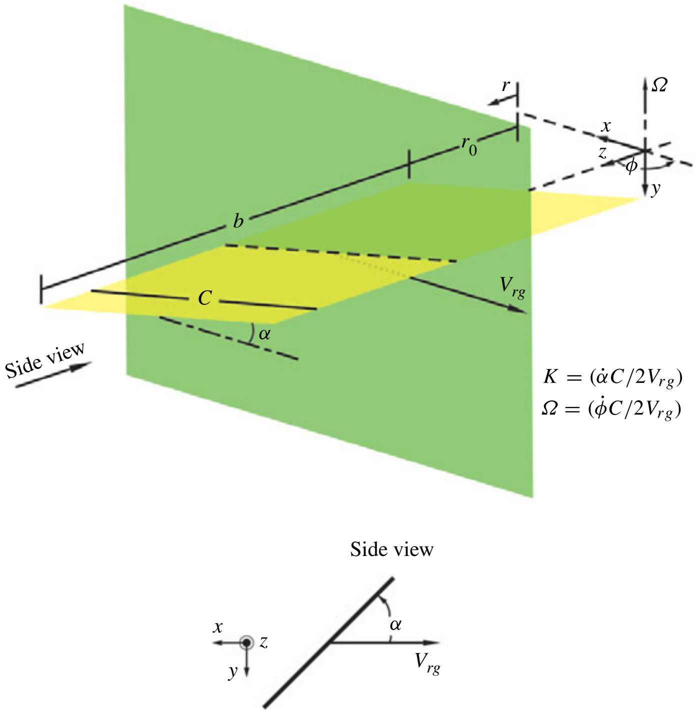

FIGURE 1. (Colour online) Schematic of rotating–pitching wing and related parameters.

Wang (2010), was used at the beginning and end of the linear ramp-up motion to avoid possible vibration and transient effects. The side view of the wing in figure 1 (bottom schematic) shows the linear velocity in the plane of rotation of the wing V_{rg} at the radius of gyration and the angle of attack α. Also displayed in the side view are the positive directions of the x, y, and z axes.

The flow structure due to pure pitch-up of the wing provides a basis for comparison of the flow patterns arising from pure rotation and simultaneous pitch-up and rotation. The quantitative images from the pure pitch-up experiments of Yilmaz (2011) and Yilmaz & Rockwell (2012) are employed for this comparison. In their experiments, the Reynolds number based on the velocity is $Re = UC/\nu = 10\,000$, in which U is the free-stream velocity incident upon the nominally stationary (non-translating) pitching wing, C is the wing chord and ν is kinematic viscosity. This value of Re is close to the aforementioned Reynolds number of $Re = 11\,776$; previous experiments of Ozen & Rockwell (2011) indicate insensitivity of the flow structure on a rotating wing to variations of Re over this range. Moreover, the reduced dimensionless pitch rate for pure pitching is $K = 0.098$; this value provides a reference pitch rate for the present experiments. Herein, the pitch rate of the wing undergoing simultaneous rotation has values less than, equal to, and greater than the non-dimensional rotation rate, $\Omega = 0.261$. Due to the large-amplitude unsteady motion, the very early development of the flow structure will be dominated by the flow pattern induced by the pitch-up manoeuvre. The current case of a stationary pitching wing with incident free stream will therefore exhibit flow structure very similar to that on an impulsively translating pitching wing when a reference frame transformation is employed.

Quantitative imaging via angular displacement SPIV was used to determine the three-dimensional velocity field. In order to employ SPIV, the water was seeded with 12 μm hollow metallic-coated plastic spheres, providing 15–20 particle images in the interrogation window size of 32 pixel × 32 pixel. A 1 mm thick laser sheet was produced by a dual-pulsed Nd-YAG operating at 14.29 Hz. Images were acquired with a camera system having a CCD array of 1600 pixel × 1200 pixel. Image pairs were acquired at an effective chordwise magnification for combined pitch-up–rotation of 9.088 and 9.482 pixels mm^{-1} for pure rotation. The acquired images were evaluated using a cross-correlation technique with 50 % overlap, yielding 5856 and 6262 vectors in the field of view for the combined pitch-up–rotation and pure rotation respectively.

Image acquisition at the midspan of the wing was repeated ten times and the ten instantaneous images were phase averaged to produce final images. Three-dimensional images of stacked slices of spanwise vorticity $\omega_z C/V_{rg}$ and isosurfaces of the parameter Q (defined below) involved acquisition of six instantaneous images at each location of the laser sheet along the span of the wing; these images were then phase averaged prior to construction of a three-dimensional image. In order to change the position of the laser sheet along the span of the wing, a traverse system translates the entire pitching–rotating wing assembly to successive spanwise locations. Image acquisition was performed on 46 planes for combined pitch-up and rotation and on 51 planes for pure rotation, with a spacing of $\Delta r/b = 0.024$. The spatial separation of the velocity data on the PIV imaging planes for combined pitch-up and rotation is 1.74 mm and for pure rotation it is 1.67 mm, which corresponds to a non-dimensional distance of $\Delta x/b = \Delta y/b = 0.022$ and $\Delta x/b = \Delta y/b = 0.021$ respectively. The total number of velocity vectors in the volume for combined pitch-up and rotation is 274 988 and for pure rotation 319 362.

An estimation of the in- and out-of-plane uncertainties followed procedures outlined in Adrian & Westerweel (2010), which indicated that the maximum bias error associated with the optical parameters in the experiment herein was approximately 5 % of the maximum local velocity (V_{rg}). Additionally the root-mean square (r.m.s.) random error estimation of the in-plane instantaneous velocity vectors was between 4 % and 5 % of the maximum local velocity. The out-of-plane displacement is often expressed in terms of the error ratio, i.e. the ratio of random r.m.s. error in the z direction to the random r.m.s. error in the x direction (assuming errors in the x and y directions are equivalent). Using the theoretical relationship, $\sigma_{\Delta z}/\sigma_{\Delta x} \cong \tan\theta^{-1}$ (Lawson & Wu 1997), where θ is the stereo half-angle, the error ratio is equivalent to 2.41. The estimated random r.m.s. in-plane error is $\sigma_{\Delta x} = 6.67$–6.95 μm; therefore the estimated out-of-plane random r.m.s. error is $\sigma_{\Delta z} = 16.10$–$16.79$ μm. An assessment of the uncertainty in the three-dimensional reconstruction techniques can be found in Yilmaz & Rockwell (2012).

The first group of experiments involves investigation of the flow structure at the midspan of the wing undergoing pure pitch-up, combined pitch-up and rotation, and pure rotation at sequential values of the convective time scale $\tau = tU/C$ or tV_{rg}/C. Imaging was performed from $\tau = 2$ to the cessation of the pitch-up manoeuvre at $\tau = 4$, corresponding to an angle of attack between $\alpha = 22.5^\circ$ and 45°. Additionally, imaging was performed at $\tau = 5.6$ while the wing remained at fixed angle of attack and continued to rotate. The schematics shown at the bottom of figure 2 clarify the classes of wing motion. In the second group of experiments, three-dimensional volume images are constructed at $\tau = 4$ for pure pitch-up, combined pitch-up and rotation, and pure rotation. The final set of experiments provides sectional images of flow past a wing undergoing combined pitching and rotating motions at three different pitch

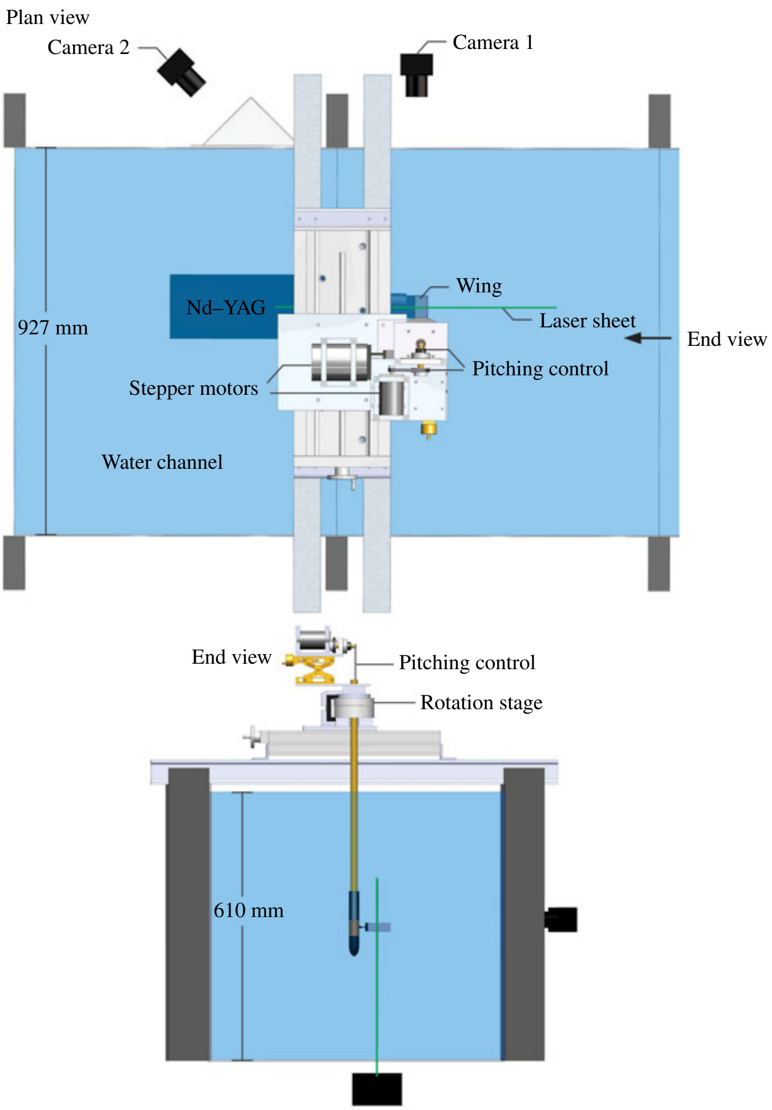

FIGURE 2. (Colour online) Schematic of rotating-pitching wing apparatus and PIV arrangement.

rates; these images are compared with those from the corresponding case of pure rotation at fixed angle of attack. In addition, images taken during relaxation of the flow structure after cessation of the pitching motion while the wing continues to rotate provide further insight.

3. Flow structure: evolution of sectional spanwise vorticity

Figure 3 shows patterns of normalized spanwise vorticity $\omega_z C/U$ and $\omega_z C/V_{rg}$ on a plane at the midspan of the wing for pure pitch-up, combined pitch-up and rotation and pure rotation. For this image, vorticity contour levels are cut off so that only vorticity pertaining to the leading edge vortex is shown. Imaging is performed at selected convective times scales during the pitching and rotation motions. In the case

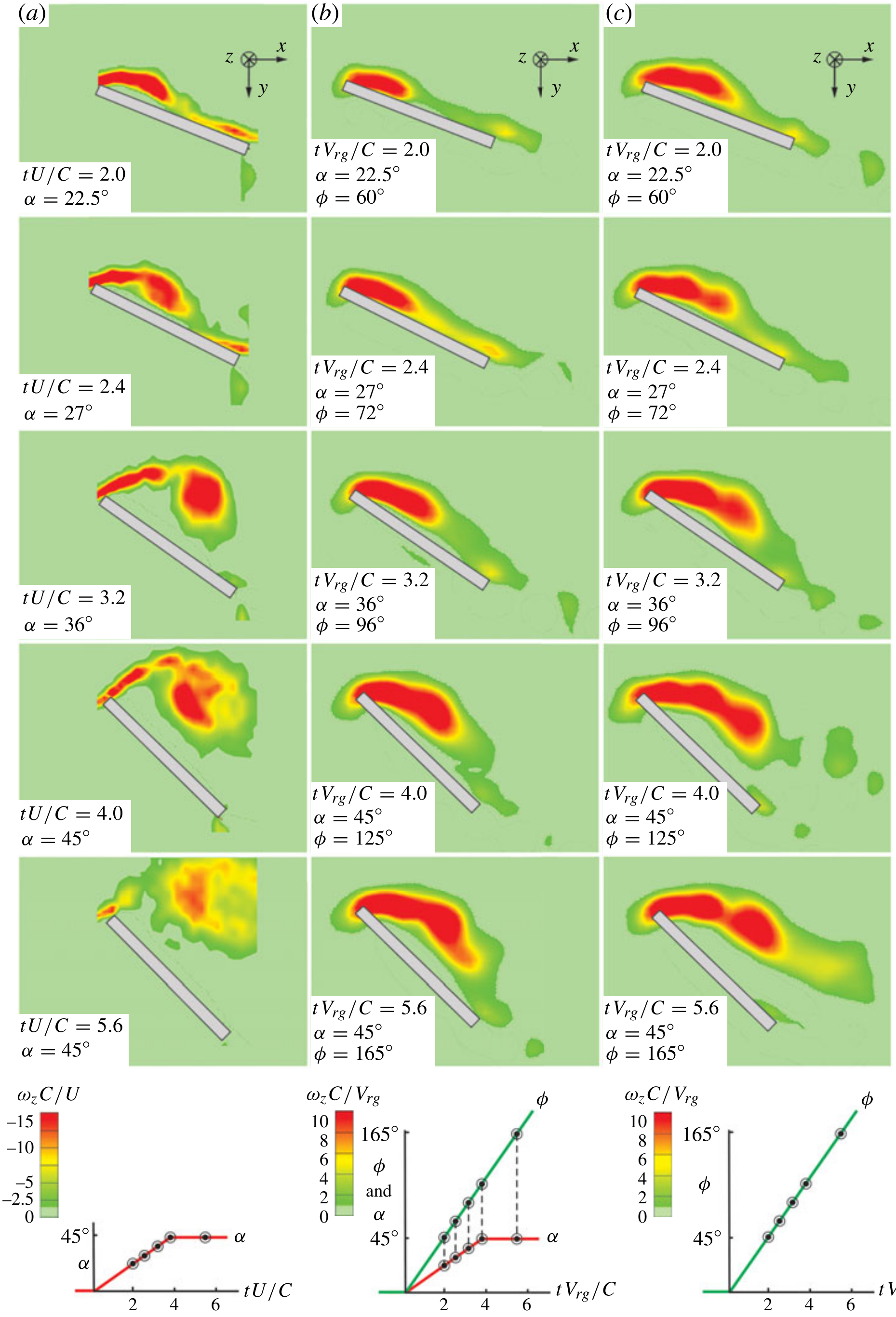

FIGURE 3. (Colour online) Sectional images of spanwise vorticity $\omega_z C/U$ and $\omega_z C/V_{rg}$ at midspan of wing for: (*a*) pure pitch-up; (*b*) pitch-up and rotation; and (*c*) pure rotation at convective times, $\tau = tU/C$ or $tV_{rg}/C = 2$, 2.4, 3.2, 4, and 5.6. Here, and in subsequent similar figures, images for pure pitch-up were determined from the data set of Yilmaz (2011).

of the pure pitch-up experiments, the wing pitches from zero angle of attack $\alpha = 0^\circ$ to $\alpha = 45^\circ$. For combined pitch-up and rotation, the wing is initially at $\alpha = 0^\circ$, and begins to pitch at the onset of rotation. Finally, the pure rotation experiments represent a wing rotating at different fixed angles of attack α. Imaging is performed for each manoeuvre at values of convective time, $\tau = 2$, 2.4, 3.2, 4, and 5.6. Images for the case of pure pitch-up in this figure, as well as in subsequent figures, are from the image data of Yilmaz (2011) and Yilmaz & Rockwell (2012).

The sectional images in figure 3(*a*) indicate that pure pitch-up gives rise to an LEV that rapidly lifts away from the surface of the wing. In contrast, as indicated in figures 3(*b*) and 3(*c*), either combined pitch-up and rotation or pure rotation stabilizes the vorticity layer at the leading edge of the wing. Of these motions, combined pitch-up and rotation yields a vorticity layer in closest proximity to the surface of the wing for all values of dimensionless time $\tau = tV_{rg}/C$. This observation is valid for imaging at the mid-span location. Three-dimensional imaging described in the subsequent sections reveals differences of the flow structure between combined pitch-up and rotation and pure rotation at the off-midplane locations. However, figure 3 demonstrates that the scale and shape of the LEV are dominated by effects due to rotation, relative to the effects of pitch-up motion.

4. Flow structure: three-dimensional patterns

4.1. *Isosurfaces of Q-criterion*

Surfaces of iso-Q correspond to constant values of the second invariant of the velocity gradient tensor as defined in Hunt, Wray & Moin (1988):

$$Q = \frac{1}{2}[\Omega_{ij}\Omega_{ij} - S_{ij}S_{ij}] = -\frac{1}{2}\frac{\partial u_i}{\partial x_j}\frac{\partial u_j}{\partial x_i}. \tag{4.1}$$

The Q-criterion indicates the magnitude of rotation relative to the amount of strain, where $\boldsymbol{\Omega}$ and $\boldsymbol{S}$ are the rotation and stress tensors respectively. When Q is positive, rotation dominates the strain; therefore, vortical structures can be identified by positive values of Q.

Figure 4 shows three-dimensional isosurfaces of the Q-criterion for pure pitch-up, combined pitch-up and rotation, and pure rotation. As indicated in figure 4(*a*), the vortical structure on the purely pitching wing is dominated by a symmetric LEV; at the midplane, the isosurface extends along the chord and arches away from the surface of the wing. This pattern was originally computed by Visbal (2011, 2012) and described experimentally by Yilmaz & Rockwell (2012). Figure 4(*b*) indicates that, in the presence of rotation, the three-dimensional vortex structure of the pitching wing is transformed to a conical, stable vortical structure along the leading edge. Moreover, a stable tip vortex also exists, along with small-scale three-dimensional structures in the wake of the wing, which wind about the tip vortex. In contrast, for the case of the rotating wing, as illustrated in figure 4(*c*), the tip vortex has degenerated, and the region of the LEV in the vicinity of the tip has also lost its coherence. Additionally, the tip-vortex structure for the combined pitch-up and rotation is in the form of one consistent structure, in contrast to the pair of structures seen on the purely rotating wing, similar to the results of Poelma *et al.* (2006).

For the case of combined pitch-up and rotation shown in figure 4(*b*), the wing motion started at $\tau = tV_{rg}/C = 0$ at $\alpha = 0^\circ$ and pitched-up simultaneously during rotation to an angle of attack $\alpha = 45^\circ$. However, the angle of attack of the purely

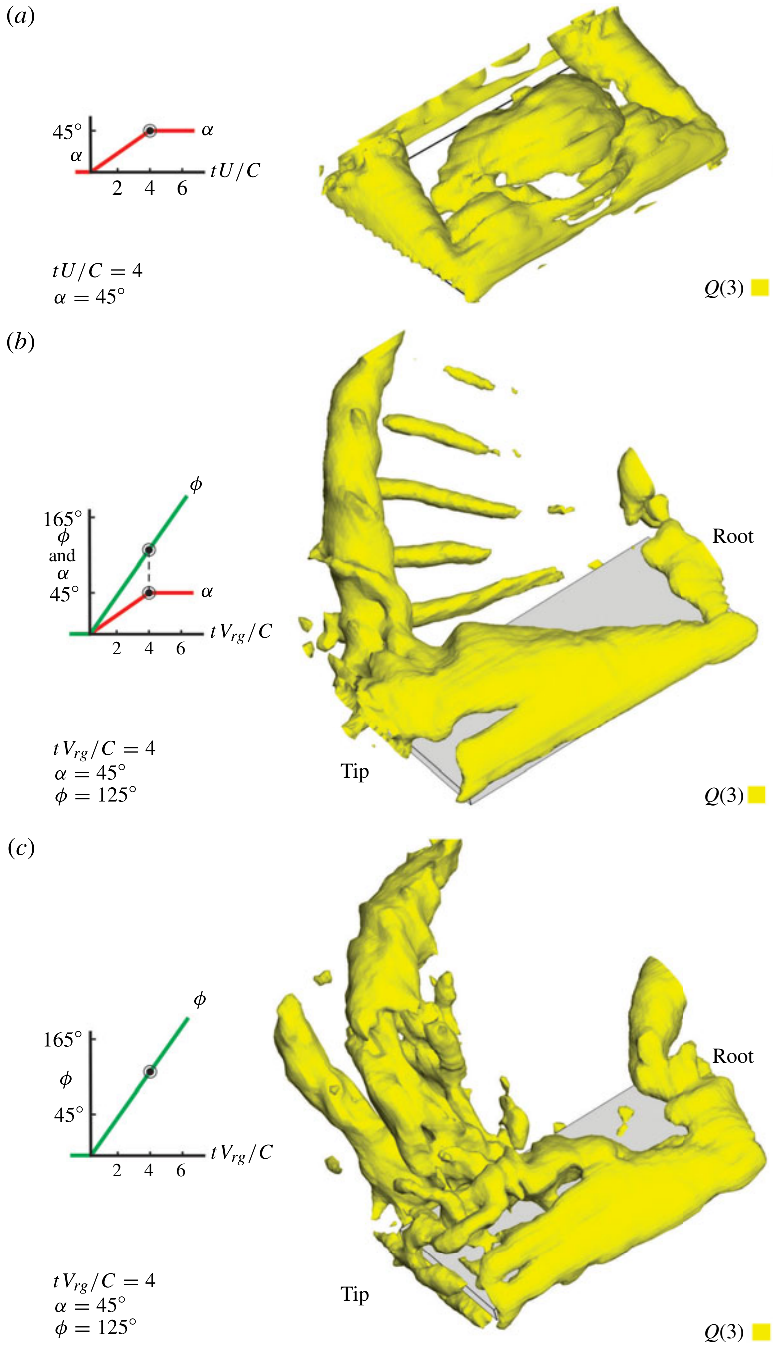

FIGURE 4. (Colour online) Isosurfaces of Q-criterion for (*a*) pure pitch-up, (*b*) pitch-up and rotation, and (*c*) pure rotation of wing.

rotating wing was maintained at $\alpha = 45^\circ$ from the onset of motion at a value of the convective time $\tau = 0$. This difference in history of the wing motion indicates an important point regarding the coherence of the tip vortex. For the kinematics and Reynolds numbers examined here, coherence is maintained if the angle of attack α is increased gradually during the pitch-up motion. On the other hand, if α is maintained constant from the onset of rotation, substantial degradation of the tip vortical structure occurs.

4.2. *Three-dimensional patterns of spanwise vorticity*

Figure 5 shows stacked sectional cuts of spanwise vorticity $\omega_z C/U$ for pure pitch-up and $\omega_z C/V_{rg}$ for combined pitch-up and rotation, and pure rotation. These sequences of patterns of spanwise vorticity along the span of the wing further indicate the coherence of the vortex structure, or lack thereof. For the case of the wing undergoing pure pitch-up, as well as the wing experiencing combined pitch-up and rotation, the structure of the LEV is well organized. Moreover, for the case of combined pitch-up and rotation, the structure of both the spanwise-oriented (negative) vorticity and small-scale structures in the wake region are highly ordered. The small-scale vortices from the trailing edge suggest the existence of a short-wavelength Kelvin–Helmholtz instability. In contrast, as evident in figure 6 below, for the case of the rotating wing, the LEV, as well as the vorticity from the trailing edge of the wing, show substantial loss of coherence, i.e. relatively strong disorder. This interpretation is based on the surfaces of iso-Q, which account for all three components of vorticity. On the other hand, as indicated in figure 5, which shows slices of only spanwise vorticity, such degradation of coherence is not evident at the leading edge, but is indicated in the vortical structures from the trailing edge of the wing.

4.3. *Helicity and three-dimensional streamline patterns*

Figure 6 displays three-dimensional streamlines and (coloured) helical density on iso-Q surfaces for a wing undergoing pure pitch-up, combined pitch-up and rotation, and pure rotation. These images are displayed in the fluid-at-infinity reference frame (fluid at rest at infinity). The helical density, h, or helicity per unit volume, is calculated by taking the scalar product of the three-dimensional velocity field $\boldsymbol{V}$ and the three-dimensional vorticity field $\boldsymbol{\omega}$ (Moffatt 1969), i.e. $h = (\boldsymbol{V} \boldsymbol{\cdot} \boldsymbol{\omega})$. Helical density indicates to what degree a flow structure is three-dimensional and serves as an indicator of vorticity flux on the primary axis of the vortex (Moffatt 1969; Le *et al.* 2011; Carr *et al.* 2013).

As shown in figure 6(*a*), values of h on the purely pitching wing have opposite signs, i.e. positive and negative colouring, on either side of the midplane of the wing, extending to a region ahead of the arch vortex. These contours indicate strong spanwise flow directed outboard from the plane of symmetry on either side of the arch vortex. For the combined pitching and rotating wing, a relatively large extent of positive h persists near the root of the LEV. For the purely rotating wing, however, the spatial extent is much smaller in the same region of the LEV. Correspondingly, the iso-Q surface that represents the LEV has degenerated into a form involving several finger-like iso-Q surfaces along and downstream of the leading edge. In essence, the larger extent of helicity close to the root of the LEV on the wing undergoing simultaneous pitch-up and rotation is correlated with preservation of the integrity of the entire LEV. Degradation of the LEV for pure rotation is associated with the smaller concentration of positive helicity close to the root of the wing.

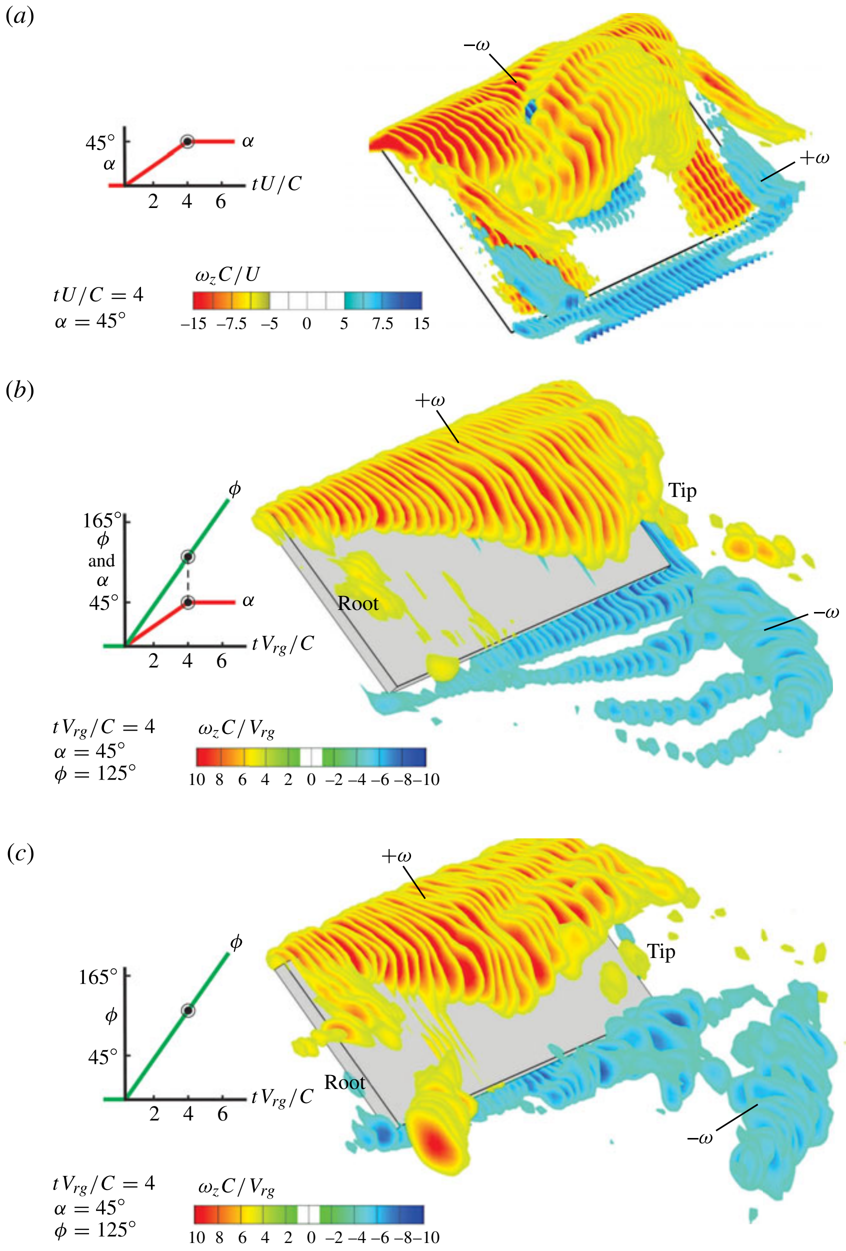

FIGURE 5. (Colour online) Sectional images of spanwise-oriented vorticity, $\omega_z C/U$ and $\omega_z C/V_{rg}$ along span of wing undergoing (*a*) pure pitch-up, (*b*) pitch-up and rotation, and (*c*) pure rotation.

Regarding the structure of the tip vortices for the various types of wing motion shown in figure 6, consider first the case of pure pitch-up (figure 6*a*). For both of the tip vortices, high levels of positive and negative helicity h occur, indicating upstream flow through the vortex cores. For simultaneous pitch-up and rotation, shown in figure 6(*b*), the highly coherent tip vortex shows a region of large negative h on the

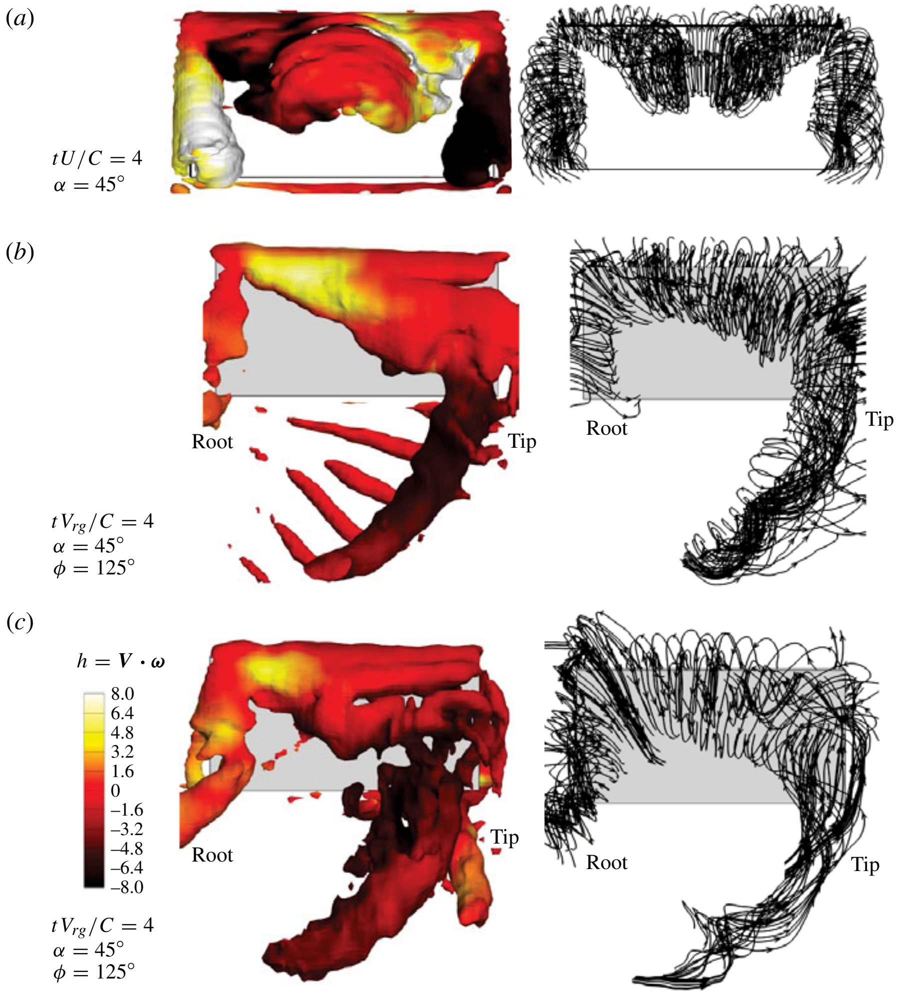

FIGURE 6. (Colour online) Streamlines and coloured helical density h on iso-Q surfaces for a flat plate undergoing (*a*) pure pitch-up, (*b*) pitch-up and rotation, and (*c*) pure rotation.

iso-Q surface. Physically, this observation indicates a relatively large magnitude of the vector $\boldsymbol{V}$ oriented in a direction opposite to the primary axis of the vorticity vector $\boldsymbol{\omega}$. The purely rotating wing (figure 6*c*) also has concentrations of negative h in the tip region; however, in this case, the onset of negative h occurs in the region where the tip vortex becomes disorganized or incoherent. Furthermore, the largest value of h extends only over a fraction of the diameter of the incoherent tip vortex.

The corresponding representations of three-dimensional streamlines given in figure 6 further characterize the flow structure along the span of the wing for each type of manoeuvre. For the case of pure pitch-up, streamlines are directed upstream through the cores of the tip vortices; moreover, streamlines are directed outboard from the plane of symmetry through the core of the LEV. For combined pitch-up and rotation, the streamlines are in accord with the well-organized conical LEV and the tip vortex represented by the corresponding patterns of iso-Q and h. For the wing undergoing pure rotation, the corresponding streamlines indicate less organized and distorted leading-edge and tip vortices. For the case of combined pitch-up and rotation, the well-defined swirl of the tip vortex in the wake of the wing contrasts with the case of pure rotation, where the prominent feature is weak swirl, accompanied by flow in the upstream direction towards the leading edge. This observation is consistent with the different patterns of helical density in the tip vortex of the combined pitching and rotating wing compared to the wing in pure rotation.

Taken together, all of the foregoing representations of patterns of iso-Q, helicity, and streamlines indicate the global influence of the simultaneous pitch-up and rotation of the wing, relative to the case of pure rotation. That is, enhanced magnitude and spatial extent of helicity and degree of organization of the streamline patterns extend all the way from the root region of the LEV to the trailing region of the tip vortex. In the following, sectional representations of the flow structure are provided.

5. Flow structure: sectional representations

5.1. *Sectional patterns of spanwise vorticity*

Figure 7 shows selected sectional slices of spanwise vorticity along the span of purely pitching, combined pitching and rotating, and purely rotating wings. The wing geometry in these images is stretched in the z direction, in order to clearly display the vortex structure of the selected sectional slices. The range of dimensionless vorticity contour levels and incremental values are: for pure pitch-up, $\omega_z C/U = -20$ to 2.8; with $\Delta(\omega_z C/U) = 1.2$, and for combined pitch-up and rotation, as well as pure rotation, $\omega_z C/V_{rg} = -10$ to 21.2 with $\Delta(\omega_z C/V_{rg}) = 1.2$.

For pure pitch-up, as shown in figure 7(*a*), the scale of the LEV increases from the tip of the wing towards the plane of symmetry. At the plane of symmetry (plane D), the LEV arches away from the surface of the wing. In the presence of rotation, i.e. combined pitch-up and rotation and pure rotation, which is represented by figure 7(*b*), the structure of the LEV takes the form of an elongated pattern of vorticity, in comparison with the aforementioned vorticity concentration arising from pure pitch-up motion of the wing. This elongated pattern increases in scale and begins to lift away from the surface of the wing, with increasing distance along the span, i.e. from the root to the tip. This trend is more severe for the case of pure rotation shown in figure 7(*c*), relative to the case of combined pitch-up and rotation, i.e. the vorticity layers are deflected away from the surface of the wing to a larger degree at larger spanwise distances from the root. This enhanced outward deflection of the vorticity layers for the case of pure rotation occurs in conjunction with loss of organization, or coherence, of the three-dimensional structure of the LEV as the tip is approached, illustrated by the isosurfaces of figures 4 and 6. On the other hand, vorticity layers remaining closer to the surface of the wing during combined rotation and pitching is associated with retention of the coherent structure of the LEV in figures 4 and 6.

5.2. *Sectional downwash*

Figure 8 shows sectional contours of the v-component of velocity, which is normal to the linear velocity in the plane of rotation of the wing, as indicated in the schematics. These contours are superposed on the sectional images of spanwise-oriented vorticity along the spans of wings undergoing pure pitch-up, combined pitch-up and rotation, and pure rotation, described in figure 7.

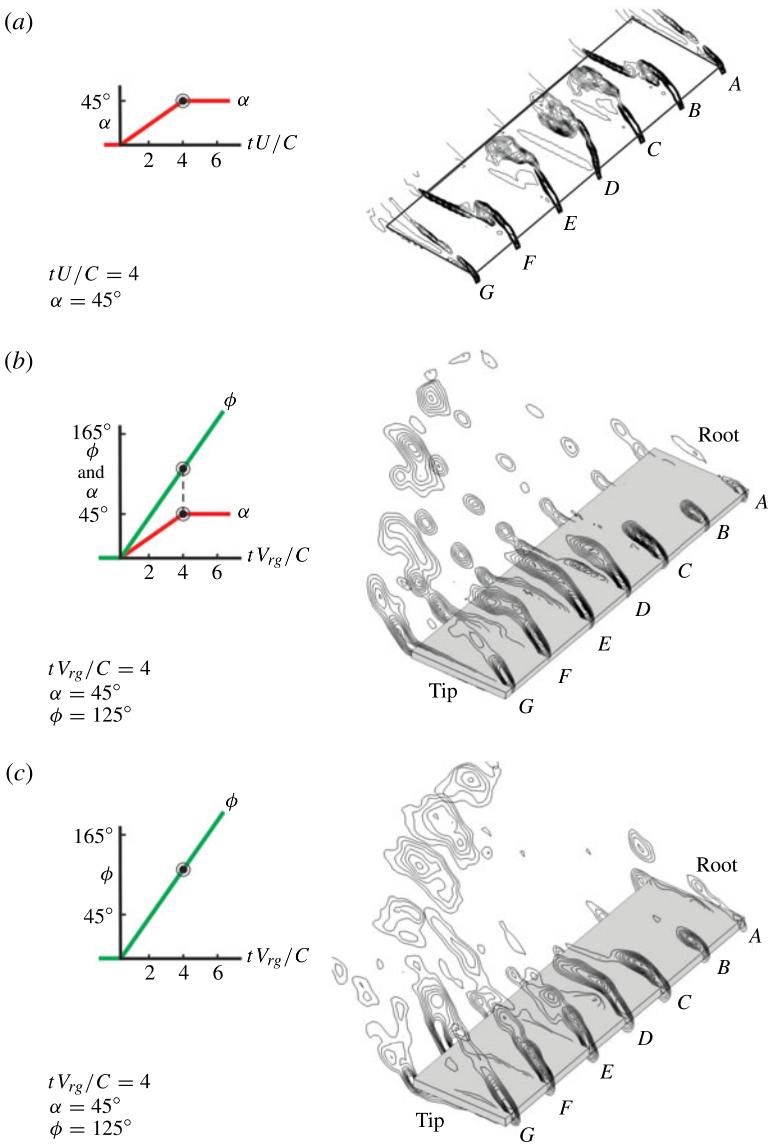

FIGURE 7. (Colour online) Sectional images of spanwise-oriented vorticity, $\omega_z C/U$ and $\omega_z C/V_{rg}$ along span of wing undergoing (*a*) pure pitch-up, (*b*) pitch-up and rotation, and (*c*) pure rotation.

For pure pitch-up, as shown in figure 8(*a*), the scale of concentrations of positive v-velocity, i.e. downwash, diminishes from the tips of the wings towards the plane of symmetry. The edge of large-magnitude downwash at each sectional location is coincident with the edge of the vorticity concentration of the LEV, despite the increase in scale and proximity to the wing surface of the LEV near the plane of symmetry. In the presence of rotation, as indicated in figures 8(*b*) and 8(*c*), the change of character of the LEV influences the distribution of the v-component along the span. For the combined pitch-up and rotation manoeuvre

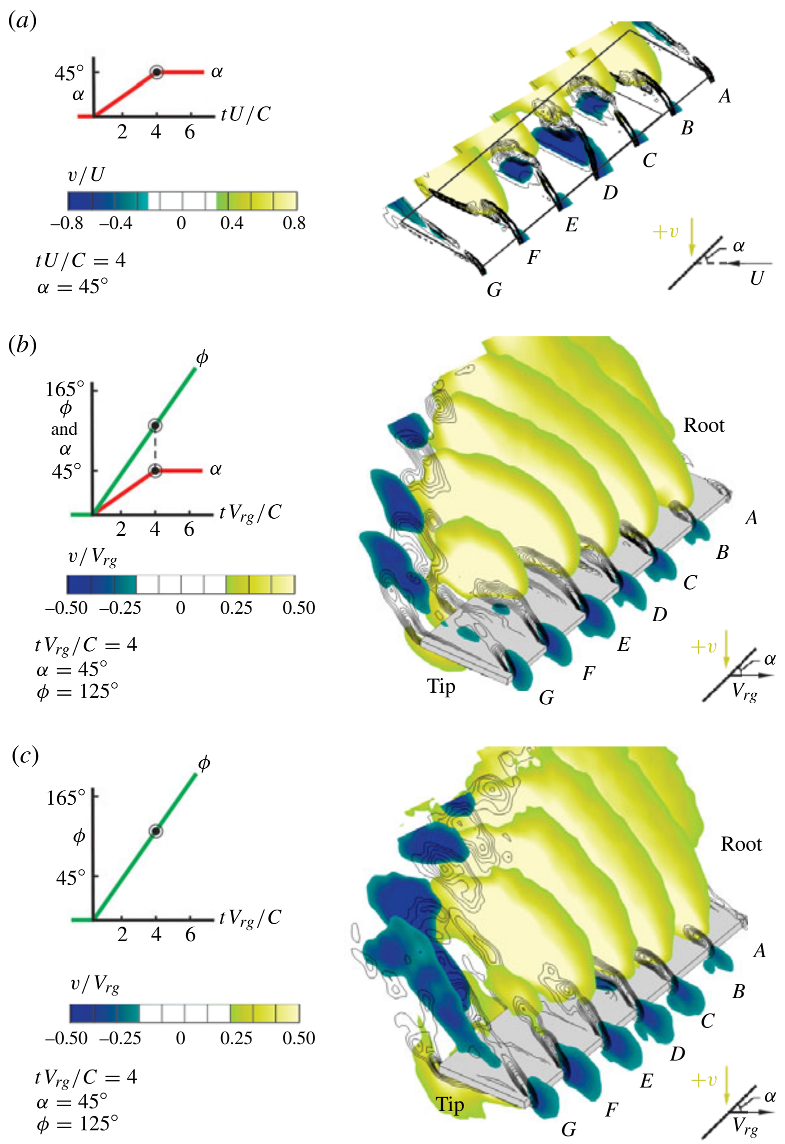

FIGURE 8. (Colour online) Sectional (colour) contours of v-component of velocity superposed on sectional (black line) contours of spanwise-oriented vorticity, $\omega_z C/U$ and $\omega_z C/V_{rg}$ along span of wing undergoing (*a*) pure pitch-up, (*b*) pitch-up and rotation, and (*c*) rotation.

(figure 8*b*), large-scale positive levels of v-component (downwash) persist along the span, and close to the leading edge, of the wing until plane F. Starting on plane D, the downwash concentration begins to diminish in scale, decreasing successively to a smaller scale on planes E and F, and eventually is not detectable on plane G, corresponding to the tip of the wing. Moreover, smaller-scale clusters of negative v-component (upwash) exist in the region of the trailing edge on planes E, F, and G. They are located adjacent to the slices of concentrated vorticity that represent the tip vortex, which is deflected across the wake, as shown in figure 4. In fact, the concentrations of downwash on planes *D*, *E*, and *F* are bounded on one side by the slices of vorticity concentration of the deflected tip vortex (located downstream of the trailing edge) and on the other side by the LEV. Additionally, the presence of this large-scale concentration of downwash downstream of the leading edge suggests a relationship between the two components, i.e. the large-scale concentrations of downwash are consistent with proximity of the vortex structure to the leading edge of the wing.

For pure rotation, shown in figure 8(*c*), generally similar patterns of downwash and upwash occur in relation to the slices of spanwise vorticity of the LEV and the tip vortex that is deflected across the wake. Slight distinctions do occur, however, relative to the foregoing case of combined pitch-up and rotation. Downwash persists as a large-scale region from the root of the wing to plane *E* to a location slightly beyond the midplane of the wing. Similarly to the case of combined pitch-up and rotation, the downwash concentrations on planes *D* and *E* appear to be bounded by the leading-edge and tip vortices. The sectional pattern of vorticity from the leading edge is detected well away from the surface of the wing on plane *F*; correspondingly, the concentration of downwash disappears, suggesting that the presence of downwash in proximity to the LEV is consistent with vortex coherence as in the case of combined pitch-up and rotation. Furthermore, concentrations of upwash are evident in plane *E* and become more pronounced in planes *F* and *G*. Despite the relative loss of coherence, i.e. onset of disorder, of the system of the leading-edge and tip vortices for the case of pure rotation, the sectional representations of downwash are qualitatively similar to the case of combined pitch-up and rotation.

5.3. *Sectional spanwise-oriented velocity*

Figure 9 shows sectional contours of the w (spanwise) component of the velocity field superposed on sectional vorticity contours at the locations indicated *A* to *G* along the span of the wing. Figures 9(*a*), 9(*b*) and 9(*c*) correspond respectively to pitch-up, combined pitch-up and rotation, and rotation.

For the case of pure pitch-up (figure 9*a*), the spanwise velocity component w is always oriented towards the plane of symmetry of the wing. Correspondingly, concentrations of positive and negative w-component are located on either side of the midplane of the wing. This representation is compatible with the streamline representation in figure 6, which shows counter-rotating swirl patterns having a component parallel to the surface of the wing.

For the combined pitch-up and rotation case (figure 9*b*), regions of positive spanwise flow are present on all planes extending from *A* to *G*. As the scale of the sectional pattern of vorticity increases at successive planes *A* to *D* along the span, the sectional concentrations of positive w-component move further downstream and extend well into the wake. On the other hand, on planes *E* to *G*, the concentrations of positive w-component are coincident with the sectional vorticity concentrations of the tip vortex that is deflected across the wake (compare the iso-Q image of figure 4). As concentrations of positive w-component move downstream of the leading edge in planes *E*, *F*, and *G*, patterns of negative w-component form near the leading edge; they indicate induced flow from the tip vortex in the negative z direction towards the root of the wing.

For pure rotation (figure 9*c*), the patterns of spanwise velocity are broadly similar to the foregoing case of pitch-up and rotation, but some distinctions are evident. On

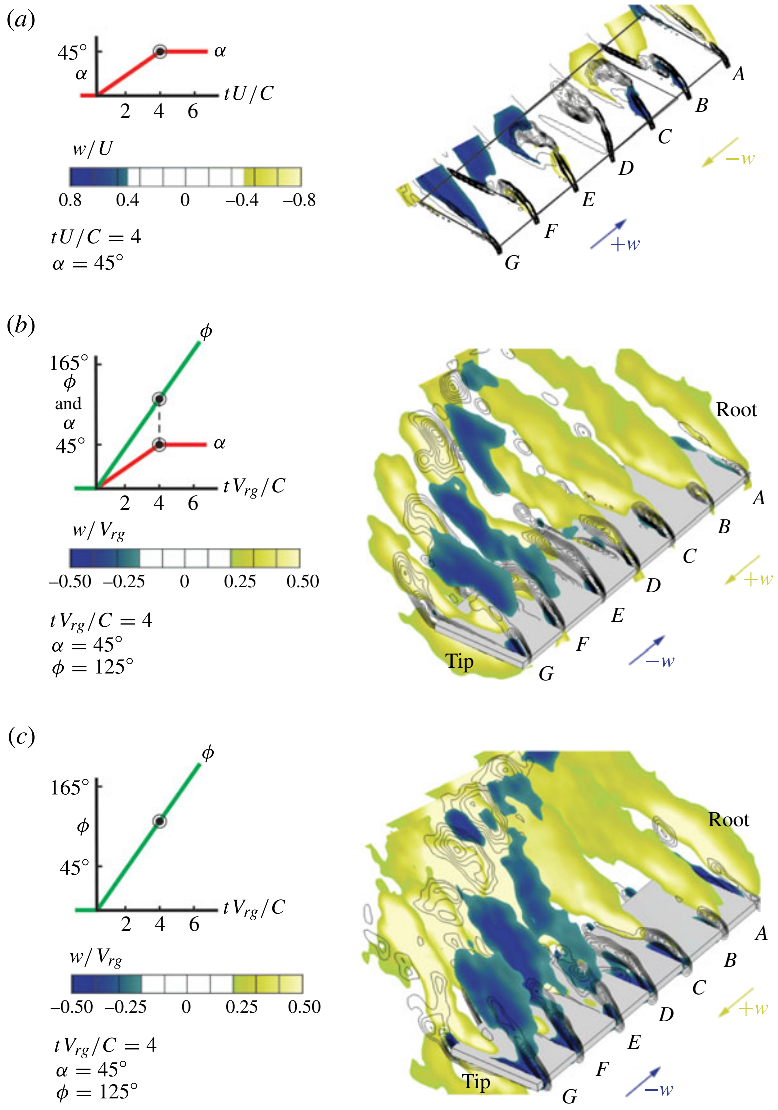

FIGURE 9. (Colour online) Sectional (colour) contours of w- (spanwise) component of velocity superposed on sectional (black line) contours of spanwise-oriented vorticity, $\omega_z C/U$ and $\omega_z C/V_{rg}$ along span of wing undergoing (*a*) pure pitch-up, (*b*) pitch-up and rotation, and (*c*) pure rotation.

planes D to G, only concentrations of negative w-component are associated with the sectional patterns of vorticity of the LEV, and both the sectional vorticity layers and the regions of negative w-component are deflected further above the surface of the wing than for the case of pitch-up and rotation shown in figure 9(*b*). As the LEV begins to deflect from the surface of the wing, significant negative concentrations of w develop in planes E, F, and G. This enhanced extent of the region of negative w is associated with the onset of disorder, i.e. loss of coherence, at the junction of the LEV and the tip vortex, as shown by the surface of iso-Q in figure 4.

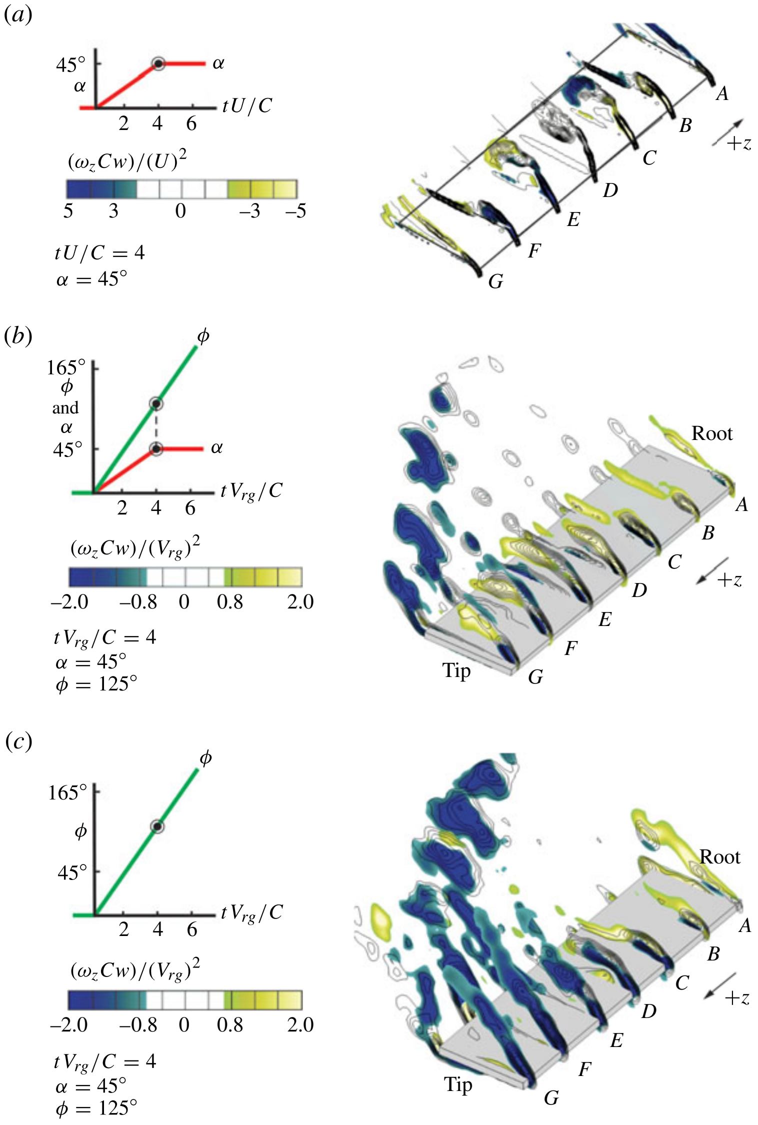

FIGURE 10. (Colour online) Sectional (colour) contours of spanwise vorticity flux, $\omega_z Cw/(U)^2$ and $\omega_z Cw/(V_{rg})^2$ superposed on sectional (black line) contours of spanwise-oriented vorticity, $\omega_z C/U$ and $\omega_z C/V_{rg}$ along span of wing undergoing (*a*) pure pitch-up, (*b*) pitch-up and rotation, and (*c*) pure rotation.

5.4. *Sectional spanwise-oriented vorticity flux*

Figure 10 shows sectional contours of spanwise vorticity flux, $\omega_z Cw/(U)^2$ and $\omega_z Cw/(V_{rg})^2$ superposed on sectional contours of spanwise-oriented vorticity along the spans of wings undergoing pure pitch-up, combined pitch-up and rotation, and pure rotation.

For the case of pure pitch-up (figure 10*a*), positive and negative regions of spanwise vorticity flux occur at sections where the LEV is relatively concentrated and remains close to the surface of the wing, i.e. planes *B* and *F*. On planes *C* and *E*, negative and positive flux occur along the trailing portion of the vorticity concentration of the sectional cut of the LEV. Moreover, the flux is zero along the plane of symmetry of the wing, i.e. plane *D*.

For the combined pitch-up and rotation manoeuvre (figure 10*b*), positive concentrations of spanwise vorticity flux exist on planes *A* to *F* where the sectional cut of vorticity is well organized and remains close to the surface of the wing. On these planes, concentrations of positive flux coincide with the core of the LEV. This persistence of positive flux across the entire span of the wing, especially in the region extending from the midspan to the tip, is associated with the highly coherent leading-edge and tip vortices in that region, as shown in the iso-*Q* plot of figure 4. Representative previous investigations that have pointed out the existence of a stable LEV in the presence of substantial spanwise velocity along the wing include Ellington *et al.* (1996), Lentink & Dickinson (2009*b*), Ozen & Rockwell (2012) and Garmann & Visbal (2014). Garmann & Visbal (2014) interpret the stabilization of the LEV in terms of the spanwise pressure gradient and the centripetal component of acceleration; the Coriolis component of acceleration was found not to exert a significant influence. Concentrations of negative flux, associated with outboard flux of negative vorticity, form downstream from the trailing edge on planes *D* to *G* and are associated with deflection of the tip vortex across the wake, evident in the iso-*Q* patterns of figure 4.

For the wing undergoing pure rotation (figure 10*c*), positive concentrations of spanwise vorticity flux are coincident with the LEV only in planes *A*, *B*, and *C*. Starting in plane *D*, the sectional cut of the vorticity layer, which represents the LEV, elongates, and lifts away from the surface of the wing on planes *E*, *F*, and *G*. On planes *D*, *E*, *F* and *G*, only negative concentrations of flux occur. This existence of only negative flux between the midspan and the tip of the wing is associated with onset of disorder, i.e. loss of coherence, at the junction of the LEV and the tip vortex, as shown in the iso-*Q* plot of figure 4. Moreover, this negative flux associated with the LEV is complemented by negative flux in the region of the trailing edge, associated with deflection of the tip vortex across the wake.

6. Flow structure: effect of pitch rate

6.1. *Vortical structures at the leading edge and from the trailing edge*

Figure 11(*a*) shows images for combined pitch-up and rotation, where the rate of pitch-up is greater than, equal to, and less than the rate of rotation. That is, the variation of pitch rate was selected so that the wing completed the pitch-up manoeuvre at $\alpha = 45^\circ$ at values of $\tau = 1$, 1.5, and 4, where $\tau = tV_{rg}/C$; the corresponding values of reduced pitch rates $K = \dot{\alpha}C/(2V_{rg})$ are $K_1 = 0.393$, $K_2 = 0.262$, and $K_3 = 0.098$. The matching cases of pure rotation at fixed angle of attack $\alpha = 45^\circ$ are given in figure 11(*b*). To quantify the strength of the vortical structures present in figure 11, the circulation of each vortical structure was calculated by integrating the spanwise vorticity normal to a rectangular box encompassing the desired vortical structure:

$$\varGamma = \iint \omega_z \mathrm{d}x\mathrm{d}y. \tag{6.1}$$

The location of the rectangular boundary (box) was determined by a vorticity threshold, this threshold being 10 % of the maximum positive and negative contour levels. Non-zero vorticity values within the box below the threshold value were not considered for the circulation calculation. Furthermore, any significant concentrations

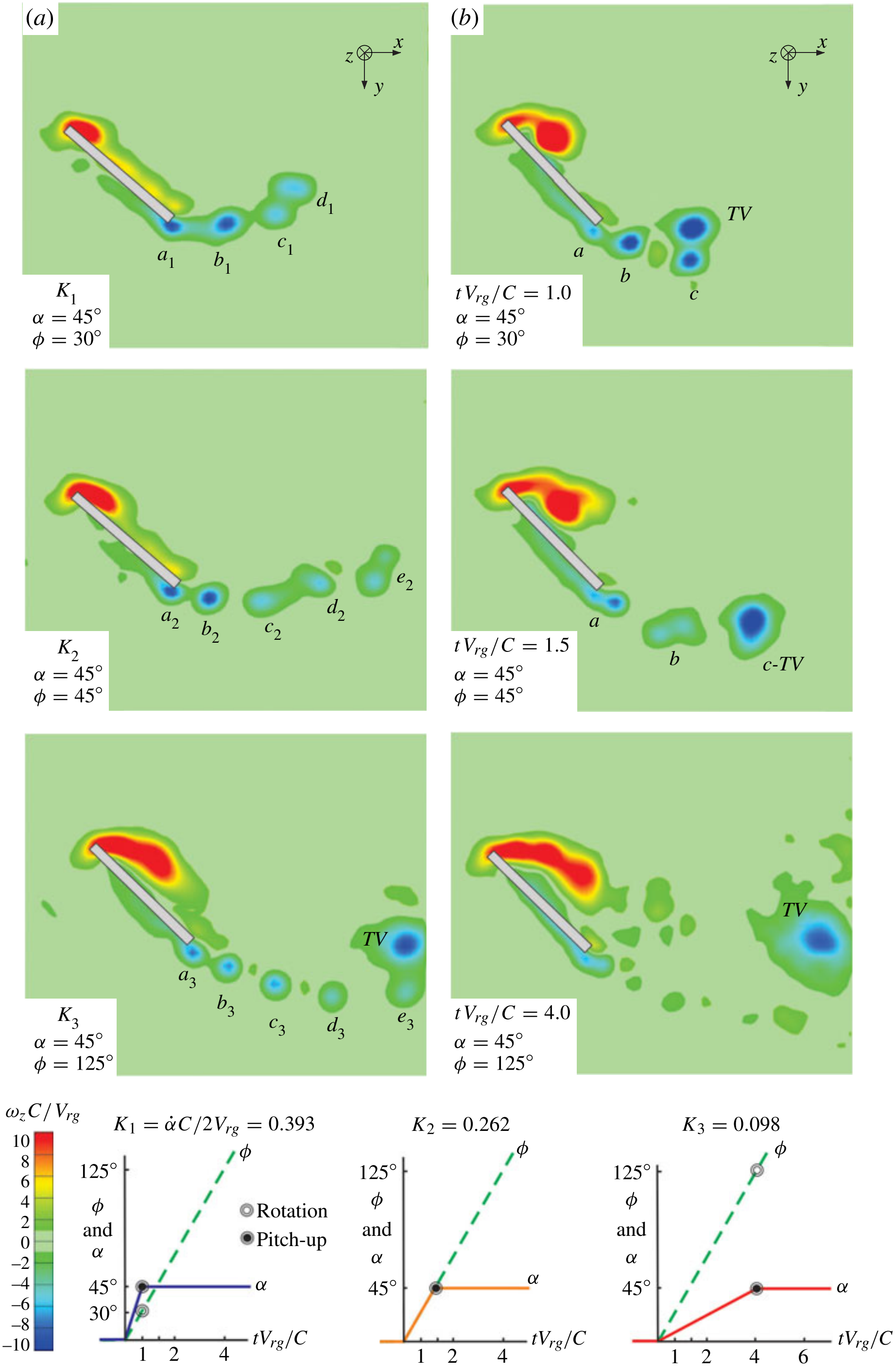

FIGURE 11. (Colour online) Sectional images of spanwise-oriented vorticity $\omega_z C/V_{rg}$ for: (*a*) simultaneous pitch-up and rotation of wing; and (*b*) pure rotation of wing at different pitch rates K.

ϕ (deg.)	Pure rotation	K_1	K_2	K_3
30	1.31	0.59	—	—
45	1.59	—	0.86	—
125	1.95	1.87	1.89	1.57
210	—	—	—	1.92

TABLE 1. Normalized positive circulation of LEV.

of negative vorticity are labeled within figure 11, leaving all unmarked vorticity on the leeward side of the wing positive.

In figure 11(*a*), it is evident that the streamwise length of the region of highest positive vorticity $\omega_z C/V_{rg}$ increases with decreasing K. This corresponds to an increase in non-dimensional circulation $\Gamma/V_{rg}C$ of the LEV, i.e. $\Gamma/V_{rg}C = 0.59$, 0.86, and 1.57 for K_1, K_2, and K_3 respectively. Positive circulation values for the LEV from §§ 6.1 and 6.2 are compiled in table 1 for reference. This general trend occurs for the corresponding cases of pure rotation given in figure 11(*b*). However, the corresponding cases of pure rotation show a distinctly different development of the structure of the LEV, if one compares images at a given value of dimensionless convective time scale τ. For combined pitch-up and rotation, where the motion starts at zero angle of attack, the vorticity layer remains closer to the surface of the wing for all time scales. The wing undergoing pure rotation, where the angle of attack is fixed at 45°, shows a vorticity layer deflected away from the wing that tends to form a vorticity concentration and has a larger overall scale than the corresponding vorticity concentration due to combined pitch-up and rotation. This observation is confirmed by the relatively larger values of circulation $\Gamma/V_{rg}C = 1.31$, 1.59, and 1.95 of the LEV at $\phi = 30°, 45°$, and 125° for pure rotation (see table 1).

Formation of concentrations of negative vorticity from the trailing edge of the wing is also influenced by the nature of the wing motion. For the case of combined pitch-up and rotation (figure 11*a*), a train, or succession of small-scale concentrations of negative vorticity, apparently due to a Kelvin–Helmholtz instability, is evident in the region downstream of the trailing edge. Similar representations of Kelvin–Helmholtz instabilities on a rotating wing were computed by Wilkins & Knowles (2007) and confirmed experimentally by Ansari *et al.* (2009).

These negative concentrations are designated by a, b, c, d and e, with subscripts 1, 2, and 3, which correspond to pitch rates K_1, K_2, and K_3. The wavelength between them is in the range $0.29C$–$0.43C$, where C is the wing chord. For the highest pitch rate K_1, the distinct structures a_1, b_1, c_1 and d_1 remain in close proximity to one another with a low-level layer of vorticity forming between each structure. With decreasing pitch rate, and hence increasing convective time of the manoeuvre, the sequence of vortices becomes more distinct and extends further into the wake of the wing, as evidenced by the vortical structures a_2, b_2, c_2, d_2, e_2 and a_3, b_3, c_3, d_3, e_3. As indicated in the bottom image of figure 11(*a*), a further type of negative vortical structure, designated as *TV*, is present. This structure is not shed from the trailing edge; rather, it is the cross-section of the tip vortex that is deflected across the wake, shown by the iso-Q surface in figure 4. The circulation of the *TV* structure in this case has a magnitude close to that of the LEV, i.e. $\Gamma/V_{rg}C(TV) = -1.62$ and $\Gamma/V_{rg}C(LEV) = 1.92$.

For pure rotation (figure 11*b*), such a well-preserved sequence of small-scale vortices does not occur. At $\tau = tV_{rg}/C = 1$, three small-scale vortices indicated by a, *b*, and *c* tend to coalesce immediately downstream of the trailing edge. At $\tau = 1.5$ concentrations *a* and *b* are distinguishable; however, *c* appears to have rolled up into the *TV* vortex structure. At $\tau = 4$, small-scale concentrations are not identifiable; only a large tip vortex *TV* is evident. The circulation of the *TV* vortex structure grows with increasing rotation angle, having values $\Gamma/V_{rg}C(30^\circ) = -0.48$, $\Gamma/V_{rg}(45^\circ) = -0.70$, and $\Gamma/V_{rg}C(125^\circ) = -1.41$.

6.2. *Relaxation of vortical structures*

Figure 12 illustrates the relaxation of flow after the pitching motion is completed for the combined pitch-up and rotation manoeuvre for reduced pitch rates K_1, K_2, and K_3. The images in figure 12(*a*) are at the end of the pitch-up motion that terminates at $\alpha = 45^\circ$. The images in figure 12(*b*) represent the vortex structure after completion of pitching while the wing continues to rotate. The delay between the cessation of the pitch-up motion (12*a*) and the acquisition of each image (12*b*) is maintained constant at values in the window of $\phi = 85^\circ$–95°, corresponding to the window of convective time of $\tau = tV_{rg}/C = 2.5$–3. Furthermore, any significant concentrations of negative vorticity are labeled within figure 11, leaving all unmarked vorticity on the leeward side of the wing positive.

It is evident that, despite the substantial differences of rate of pitch-up and the corresponding distinctions of the flow structure given in figure 12(*a*), the relaxation process gives rise to broadly similar, extended regions of vorticity concentrations. Of particular note, after the relaxation process, the sequence of vortical structures from the trailing edge, denoted by a_1, b_1, c_1, and d_1 in figure 12(*a*), appear to have rolled up into the cross-sectional tip vortex *TV*, designated in figure 12(*b*).

The circulation of the LEV shown in the images in figure 12(*a*), compared to the images in 12(*b*), further exemplifies the relaxation process. Namely, the circulation of the LEV corresponding to figure 12(*a*) increases with decreasing *K*, i.e. $\Gamma/V_{rg}C = 0.59$ at K_1, $\Gamma/V_{rg}C(K_2) = 0.86$, and $\Gamma/V_{rg}C(K_3) = 1.57$. After relaxation, however, the strength of the LEV in figure 12(*b*) is very similar, i.e. $\Gamma/V_{rg}C(K_1) = 1.87$, $\Gamma/V_{rg}C(K_2) = 1.89$, and $\Gamma/V_{rg}C(K_3) = 1.92$, despite the different initial conditions (see table 1 for reference). Similarly, the strength of the negative vortex agglomerations designated by *TV* in figure 12(*b*) are comparable, $\Gamma/V_{rg}C(K_1) = -1.62$, $\Gamma/V_{rg}C(K_2) = -1.32$, and $\Gamma/V_{rg}C(K_3) = -1.32$.

Despite large variation of the pitch-up rate relative to the rotation rate of the wing, the foregoing observations indicate that a common state of the flow structure, both at the leading edge and from the trailing edge, is rapidly attained after cessation of the pitch-up motion. This relaxation process occurs within a time scale corresponding to a few chords of wing travel. The onset of the common state is thereby insensitive to the time scale of the pitch-up motion of the wing at the beginning of wing motion. Rotational effects, more specifically centripetal acceleration and spanwise pressure gradients, prevail once the pitch-up motion has terminated. For each case of combined pitch-up and rotation, the rotation rate is the same, explaining the similar relaxation process.

7. Conclusions

The flow patterns due to pure pitch-up and pure rotational motions of a wing have been addressed extensively in previous investigations. Very little is understood, however, of the flow structure on a wing subjected to simultaneous pitching and rotation, which is the subject of the present investigation. The new flow physics

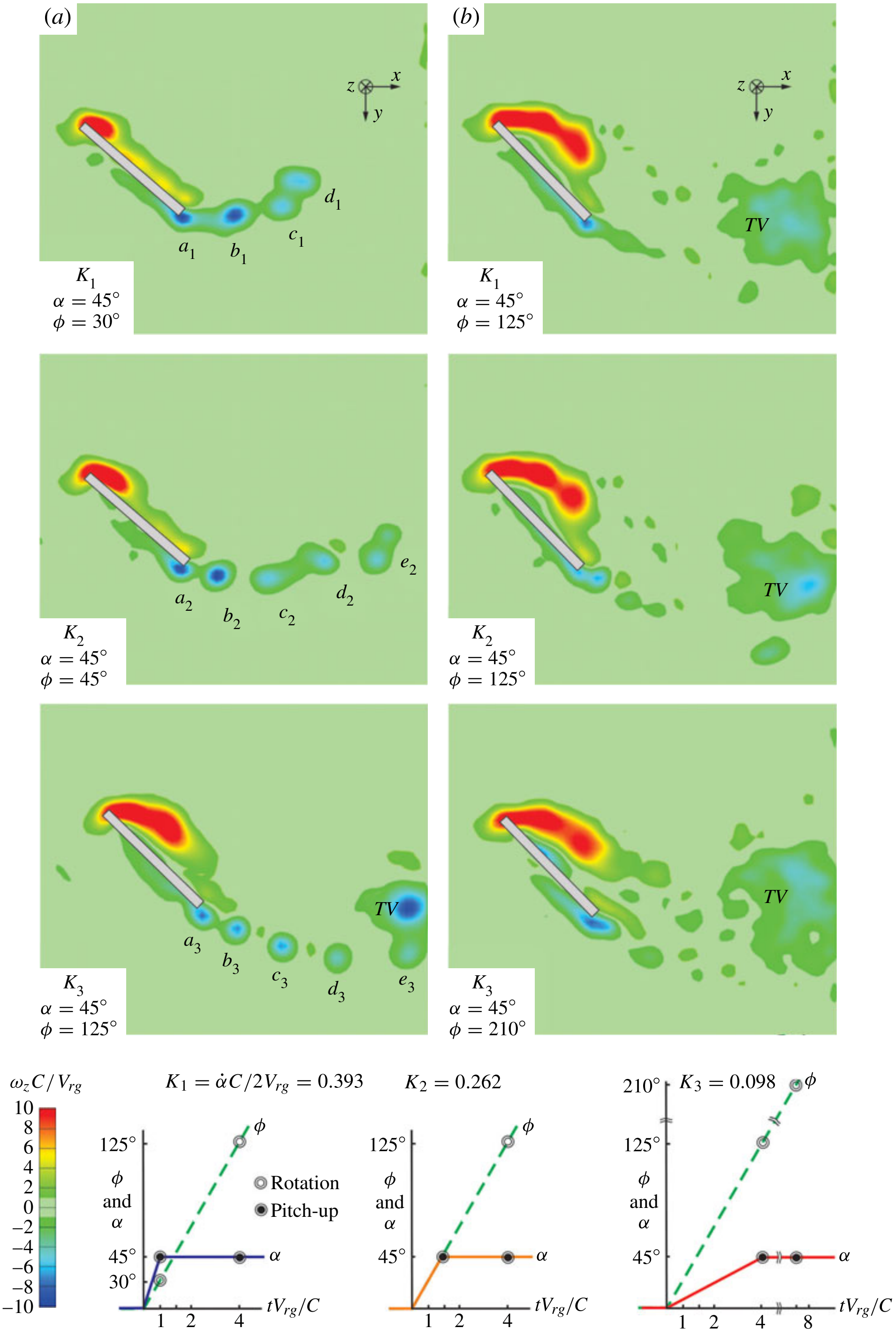

FIGURE 12. (Colour online) Sectional images of spanwise-oriented vorticity, $\omega_z C/V_{rg}$ at midspan of wing for simultaneous pitch-up and rotation: (*a*) at end of pitch-up motion; and (*b*) subsequent relaxation after end of pitch-up motion.

revealed herein for these simultaneous motions includes: stabilization of the large-scale vortex generated at the leading edge; preservation of a coherent tip-vortex–LEV system; generation of a highly ordered vortex system from the trailing edge of the wing; and rapid relaxation of the flow structure to a common state upon termination of the pitch-up component of the simultaneous pitch-up and rotational motions of the wing. The specifics of these concepts are summarized in the following.

7.1. *Effects of rotation on the flow structure induced by pitch-up motion of a wing*

The pitch-up motion of a wing is a classic manoeuvre that gives rise to a large-scale LEV, which moves away from the wing and in the downstream direction with increasing time. If the wing has a small aspect ratio, formation of the LEV takes the form of an arch vortex, and at the plane of symmetry of the wing the large-scale vortex rapidly departs from the leading edge. It is demonstrated herein that the nature of the pitch-induced vortex at the leading edge is fundamentally altered in the presence of wing rotation. That is, the LEV remains at, and close to, the surface of the leading edge of the wing with the addition of rotation.

This observation, which indicates dominance of the effects of wing rotation, is associated with the following features of flow structure. In the presence of rotation, the spanwise velocity along the wing has a large magnitude and is unidirectional, except in the tip region; this pattern of spanwise velocity contrasts with the pattern on the purely pitching wing (without rotation), where the sign of the spanwise velocity is opposite on either side of the plane of symmetry of the wing. Moreover, it is possible to attain spanwise flux of vorticity through the LEV that is unidirectional along the span of the wing for combined pitching and rotation, in contrast to the oppositely directed vorticity flux on either side of the plane of symmetry of the purely pitching wing. Finally, in the presence of rotation, patterns of large-magnitude downwash on the pitching–rotating wing extend to a region close to the leading edge, in contrast to the purely pitching wing, where they are displaced to a larger chordwise distance. All of these features contribute to the fundamental difference of the three-dimensional surfaces of iso-Q, which exhibit a conical LEV in the presence of rotation, in contrast to the arch LEV for pure pitching.

7.2. *Effects of rotation on the flow structure induced by pitch-up motion of a wing: relaxation after cessation of pitch-up*

A further indicator of the strong influence of rotation is the rapid relaxation of the flow structure upon termination of pitch-up, irrespective of the value of pitch rate. When the rate of rotation is held constant, and the pitch rate takes values less than, equal to, and greater than the rotation rate, the sectional cut of the LEV at the midspan of the wing shows different degrees of development at the end of the pitch-up motion. Yet, after only a few convective time scales of the wing rotation, the LEV evolves to a form characteristic of pure rotation of the wing over the entire range of the manoeuvre. That is, it is stable, in an elongated form, and remains close to the surface of the wing. Moreover, the circulation of the LEV at the end of this brief relaxation process has nearly the same value for all values of initial pitch rate. Likewise, the sequence of vortices from the trailing edge of the wing shows different patterns at the end of the pitch-up motion, but collapses to a similar form dominated by the deflected tip vortex at the end of relaxation. In essence, consideration of a large range of values of the pitch-up rate relative to the rotation rate of the wing shows that a common pattern of vortical structures rapidly develops after termination of the pitch-up motion. This common pattern, or state, which involves structures at the leading edge and downstream of the trailing edge, is attained within a relatively small convective time scale, corresponding to a few chords of wing travel. The onset of the common state is associated with the dominant effects of centripetal acceleration and spanwise pressure gradient due to equivalent rotation rates for each manoeuvre.

7.3. *Effects of rotation on the flow structure induced by pitch-up motion of a wing: comparison with the flow structure arising from pure rotation*

From the foregoing, it is evident that the effects of rotation have a strong influence on the flow structure during pitch-up. The distinctions between the flow structure on a wing undergoing combined pitch-up and rotation and a wing in pure rotation have been identified in the present investigation. For pure rotation, it is shown that the coherence of the tip vortex is substantially degraded at sufficiently large rotation angle. This degradation extends into the outboard region of the LEV. With simultaneous pitch-up and rotation, however, the coherence of the entire tip–LEV system is maintained. These features are evident from comparison of iso-Q surfaces. Superposed surfaces of helical density show regions of large-magnitude positive and negative helical density respectively extending across the LEV and the tip vortex for simultaneous pitch-up and rotation. Corresponding patterns of streamlines show well-defined swirl throughout the leading-edge–tip vortex system; in contrast, for pure rotation, the ordered nature of the swirl streamlines is disrupted and there is upstream flow through the disordered tip vortex.

Sectional representations of the flow structure along the span of the wing indicate that, in the region from the midspan to the tip of the wing, the effect of the combined pitch-up and rotation motion is to retain the sectional patterns of spanwise vorticity close to the surface of the wing and maintain positive vorticity flux through the regions of large spanwise vorticity, in conjunction with large-magnitude downwash extending close to the tip of the wing. None of these features are attained for the case of pure rotation of the wing.

In the region downstream of the trailing edge of the wing, patterns of vortical structures are distinctly different for the cases of simultaneous pitch-up rotation, in comparison with pure rotation. For the former, a highly ordered series of small-scale vorticity concentrations, with nearly constant wavelength between them, is formed from the trailing edge. On the other hand, for the case of pure rotation, the structure from the trailing edge is not so ordered, and the near wake is dominated by the deflected tip vortex across the wake.

Acknowledgement

The authors are pleased to acknowledge the financial support of the Air Force Office of Scientific Research under grant no. FA9550-11-1-0069 monitored by Dr D. Smith.

REFERENCES

ADRIAN, R. J. & WESTERWEEL, J. 2010 *Particle Image Velocimetry*. Cambridge University Press.

ANSARI, S. A., PHILLIPS, N., STABLER, G., WILKINS, P. C., ZBIKOWSKI, R. & KNOWLES, K. 2009 The effect of advance ratio on the aerodynamics of revolving wings. *Exp. Fluids* **46**, 777–798; and Erratum *Exp. Fluids* **51**, 2011, 571–572.

BROSS, M., OZEN, C. A. & ROCKWELL, D. 2013 Flow structure on a rotating wing: effect of steady incident flow. *Phys. Fluids* **25**.

CARR, Z., CHEN, C. & RINGUETTE, M. J. 2013 Finite-span rotating wings: three-dimensional vortex formation and variations with aspect ratio. *Exp. Fluids* **54**, 1444–1470.

CHENG, B., SANE, S. P., BARBERA, G., TROOLIN, D. R., STRAND, T. & DENG, X. 2013 Three-dimensional flow visualization and vorticity dynamics in revolving wings. *Exp. Fluids* **54**, 1423–1425.

DICKSON, W. B. & DICKINSON, M. H. 2004 The effect of advance ratio on the aerodynamics of revolving wings. *J. Expl Biol.* **207**, 4269–4281.

EKATERINARIS, J. & PLATZER, M. 1998 Computational predictions of airfoil dynamic stall. *Prog. Aerosp. Sci.* **33**, 759–846.

ELDREDGE, J. D. & WANG, C. 2010 High-fidelity simulations and low-order modeling of a rapidly pitching plate. *AIAA Paper* 2010-4281.

ELLINGTON, C. P., VAN DER BERG, C., WILLMOTT, A. P. & THOMAS, A. L. R. 1996 Leading-edge vortices in insect flight. *Nature* **384**, 19–26.

GARMANN, D. J. & VISBAL, M. R. 2011 Numerical investigation of transitional flow over a rapidly pitching plate. *Phys. Fluids* **23**, 094106.

GARMANN, D. J. & VISBAL, M. R. 2014 Dynamics of revolving wings for various aspect ratios. *J. Fluid Mech.* **686**, 451–483.

GARMANN, D. J., VISBAL, M. R. & ORKWIS, P. D. 2013 Three-dimensional flow structure and aerodynamic loading on revolving wing. *Phys. Fluids* **25**, 034101.

GRANLUND, K., OL, M. & BERNAL, L. 2011 Experiments on pitching plates: force and flowfield measurements at low Reynolds number. *AIAA Paper* 2011-872.

HARTLOPER, C., KINZEL, M. & RIVAL, D. E. 2013 On the competition between leading-edge and tip-vortex growth for a pitching plant. *Exp. Fluids* **54**, 1447–1458.

HUNT, J. C. R., WRAY, A. A. & MOIN, P. 1988 Eddies, stream, and convergence zones in turbulent flows. In *Studying Turbulence Using Numerical Simulation Databases*, vol. 2, pp. 193–208.

KIM, D. & GHARIB, M. 2010 Experimental study of three-dimensional vortex structures in translating and rotating plates. *Exp. Fluids* **49**, 329–339.

LAWSON, N. J. & WU, J. 1997 Three-dimensional particle image velocimetry: error analysis of stereoscopic techniques. *Meas. Sci. Technol.* **8**, 897–900.

LE, T. B., BORAZJANI, I., KANG, S. & SOTIROPOULOS, F. 2011 On the structure of vortex rings from inclined nozzles. *J. Fluid Mech.* **686**, 451–483.

LEHMANN, F. O. & DICKINSON, M. H. 1998 The control of wing kinematic and flight forces in fruit flies. *J. Expl Biol.* **401**, 385–401.

LENTINK, D. & DICKINSON, M. H. 2009*a* Biofluiddynamic scaling of flapping, spinning and translating fins and wings. *J. Expl Biol.* **212**, 2691–2704.

LENTINK, D. & DICKINSON, M. H. 2009*b* Rotational accelerations stabilize leading edge vortices on revolving fly wings. *J. Expl Biol.* **212**, 2705–2719.

MCCROSKEY, W. J. 1982 Unsteady airfoils. *Annu. Rev. Fluid Mech.* **14**, 285–311.

MOFFATT, H. 1969 The degree of knottedness of tangled vortex lines. *J. Fluid Mech.* **35**, 117–129.

OZEN, C. A. & ROCKWELL, D. 2011 Flow structure on a rotating plate. *Exp. Fluids* **52**, 207–223.

OZEN, C. A. & ROCKWELL, D. 2012 Three-dimensional vortex structure on a rotating wing. *J. Fluid Mech.* **748**, 932–956.

POELMA, C., DICKSON, W. B. & DICKINSON, M. H. 2006 Time-resolved reconstruction of the full velocity field around a dynamically-scaled flapping wing. *Exp. Fluids* **41**, 213–225.

SANE, S. P. 2003 The aerodynamics of insect flight. *J. Expl Biol.* **206**, 4191–4208.

SHIH, C., LOURENCO, L., VAN DOMMELEN, L. & KROTHAPALLI, A. 1992 High-fidelity simulations and low-order modeling of a rapidly pitching plate. *AIAA J.* **30**, 1153–1161.

SHYY, W., AONO, H., CHIMAKURTHI, S. K., TRIZILA, P., KANG, C.-K., CESNIK, C. E. S. & LIU, H. 2010 Recent progress in flapping wing aerodynamics and aeroelasticity. *Prog. Aerosp. Sci.* **46**, 284–327.

VISBAL, M. R. 2011 Three-dimensional flow structure on a heaving low-aspect-ratio wing. *AIAA Paper* 2011-219.

VISBAL, M. R. 2012 Flow structure and unsteady loading over a pitching and perching low-aspect-ratio wing. *AIAA Paper* 2012-3279.

VISBAL, M. R. & SHANG, J. S. 1989 Investigations of the flow structure around a rapidly pitching airfoill. *AIAA J.* **27**, 1044–1051.

WILKINS, P. & KNOWLES, K. 2007 Investigation of aerodynamics relevant to flapping-wing micro air vehicles. *AIAA Paper* 2007-4338.

WOJCIK, C. J. & BUCHHOLZ, J. H. 2014 Parameter variation and the leading-edge vortex of a rotating flat plate. *AIAA J.* **52**, 348–357.

YILMAZ, T. O. 2011 Investigation of three-dimensional flow structure on maneuvering finite-span wings. PhD thesis, Lehigh University.

YILMAZ, T., OL, M. & ROCKWELL, D. 2010 Scaling of flow separation on a pitching low aspect ratio plate. *J. Fluids Struct.* **26**, 1034–1041.

YILMAZ, T. O. & ROCKWELL, D. 2012 Flow structure on finite-span wings due to pitch-up motion. *J. Fluid Mech.* **691**, 518–545.

ZHANG, X. & SCHLUTER, J. U. 2012 Numerical study of the influence of the Reynolds-number on the lift created by a leading edge vortex. *Phys. Fluids* **24**, 065102.